# Connecting local structure, strain and ionic transport in the fast sodium ion conductor $Na_{11+x}Sn_{2+x}P_{1-x}S_{12}$

Oliver Maus<sup>[a,b]</sup>, Bibek Samanta<sup>[b,c]</sup>, Florian Schreiner<sup>[c]</sup>, Kyra Strotmann<sup>[a]</sup>, Martin A.

Lange<sup>[a,d]</sup>, Marvin A. Kraft<sup>[a,d]</sup>, Matthias Hartmann<sup>[a,b]</sup>, Niina Jalarvo<sup>[e]</sup>, Michael Ryan

Hansen<sup>[b,c]</sup>, Wolfgang G. Zeier\*<sup>[a,b,d]</sup>

<sup>a</sup>Institute of Inorganic and Analytical Chemistry, University of Münster, D-48149 Münster, Germany

bInternational Graduate School for Battery Chemistry, Characterization, Analysis, Recycling and Application (BACCARA), University of Münster, D-48149 Münster, Germany

cInstitute of Physical Chemistry, University of Münster, D-48149 Münster, Germany

d Institute of Energy Materials and Devices (IMD), IMD-4: Helmholtz-Institut Münster,
Forschungszentrum Jülich, Corrensstraße 46, D-48149 Münster, Germany

eNeutron Science Division, Oak Ridge National Laboratory, Oak Ridge, TN 37830, USA

## **Abstract**

On the road to highly performing solid electrolytes for solid state batteries, aliovalent substitution is a powerful strategy to improve the ionic conductivity. While the substitution allows optimization of the charge carrier concentration, effects on the local structure are often overlooked. Here, we show by pair distribution function analyses that partial substitution of PS<sub>4</sub><sup>3-</sup> by SnS<sub>4</sub><sup>4-</sup> polyanion in the fast sodium ionic conductor Na<sub>11+x</sub>Sn<sub>2+x</sub>P<sub>1-x</sub>S<sub>12</sub> results in discrepancies between the local and average structure. The significantly larger SnS<sub>4</sub><sup>4-</sup> polyanions lead to inhomogeneities in the local environments of sodium ions and induce micro strain in the material. The combination of nuclear magnetic resonance spectroscopy and quasielastic neutron scattering reveals a decrease in the activation energy of fast local ionic jumps. The substitution widens the bottleneck size of some diffusion pathways and a correlation between the increased strain and improved local ionic transport is observed. Local frustrations caused by the induced inhomogeneities may flatten the energy landscape and lead to the detected decrease in the activation barrier. Understanding these effects of cationic substitution on the local structure, induced crystallographic strain and ionic transport can open up new possibilities to design fast conducting solid electrolytes.

## 1. Introduction

Solid-state batteries have the potential to provide higher energy densities than the conventional lithium ion batteries based on liquid electrolytes<sup>1</sup> making them a promising technology for the electrification of vehicles and many other industry sectors. An essential part of a solid-state battery is the solid electrolyte which allows the transport of the mobile ions to the active material. Therefore, electrolytes with high ionic conductivities are necessary to enable sufficient capacities and power densities.<sup>2</sup> Li<sup>+</sup>-ion conductors in the classes of oxides<sup>3,4</sup>, halides, <sup>5,6</sup> and oxyhalides<sup>7,8</sup> have been investigated as promising materials in recent years. In particular, sulfide-based solid electrolytes have drawn much attention as compounds like Li<sub>5.5</sub>PS<sub>4.5</sub>Cl<sub>1.5</sub><sup>9</sup> and Li<sub>10</sub>GeP<sub>2</sub>S<sub>12</sub><sup>10,11</sup> reach ionic conductivities of 10 mS·cm<sup>-1</sup> and above. However, with limited lithium resources on the earth sodium solid-state batteries have gained increasing interest due to the high abundance and low cost of sodium as well as due to faster ionic transport of the less polarizing Na<sup>+</sup> ions in solid electrolytes.<sup>12</sup> Inspired by the lithium ion conductors, an increasing number of sodium solid electrolytes, such as oxides (e.g. NASICONs), <sup>13</sup> halides (e.g. Na<sub>2+x</sub>Zr<sub>1-x</sub>M<sub>x</sub>Cl<sub>6</sub>, M = Er, In, Y), <sup>14,15</sup> and oxyhalides (e.g. NaMOCl<sub>4</sub>, M = Ta, Nb)<sup>16,17</sup> have been reported over the last years.

In the field of sulfide-based sodium-ion conductors, Na<sub>3</sub>PS<sub>4</sub> represents one of the first and most studied materials. 18,19 In this structure type, the PS<sub>4</sub><sup>3-</sup> polyanions form a body-centered anion backbone where the octahedral voids are filled by sodium ions. At room temperature, the polyanions are rotated with respect to each other leading to tetragonal symmetry (space group  $P\overline{4}2_1c$ ) and two distinct sodium-ion positions. The relatively low ionic conductivity of pristine Na<sub>3</sub>PS<sub>4</sub> (0.04 mS·cm<sup>-1</sup>) can be improved by widening the bottleneck, i.e. increasing the size of the transition state of ionic jumps, with the substitution by antimony and selenium.<sup>20</sup> The selenium endmembers, Na<sub>3</sub>PSe<sub>4</sub> and Na<sub>3</sub>SbSe<sub>4</sub>, crystallize at room temperature in the cubic structure polymorph (space group  $I\overline{4}3m$ ) in which the polyanions are not rotated.<sup>21</sup> The cubic phase is also obtained when Na<sub>3</sub>PS<sub>4</sub> is prepared via mechanochemical synthesis as indicated by X-ray diffraction.<sup>22</sup> However, pair distribution function analyses show that the short-range order remains tetragonal while the introduction of defects by ball milling leads to a cubic average structure.<sup>23</sup> While aliovalent substitution in Na<sub>2.9</sub>W<sub>0.1</sub>Sb<sub>0.9</sub>S<sub>4</sub> highly improves the conductivity by introducing vacancies into the structure, 24,25 it causes a similar discrepancy between local and average structure. Here, dynamic sampling of the local tetragonal structure leads to a cubic average structure detected by X-ray diffraction at room temperature. <sup>26,27</sup>

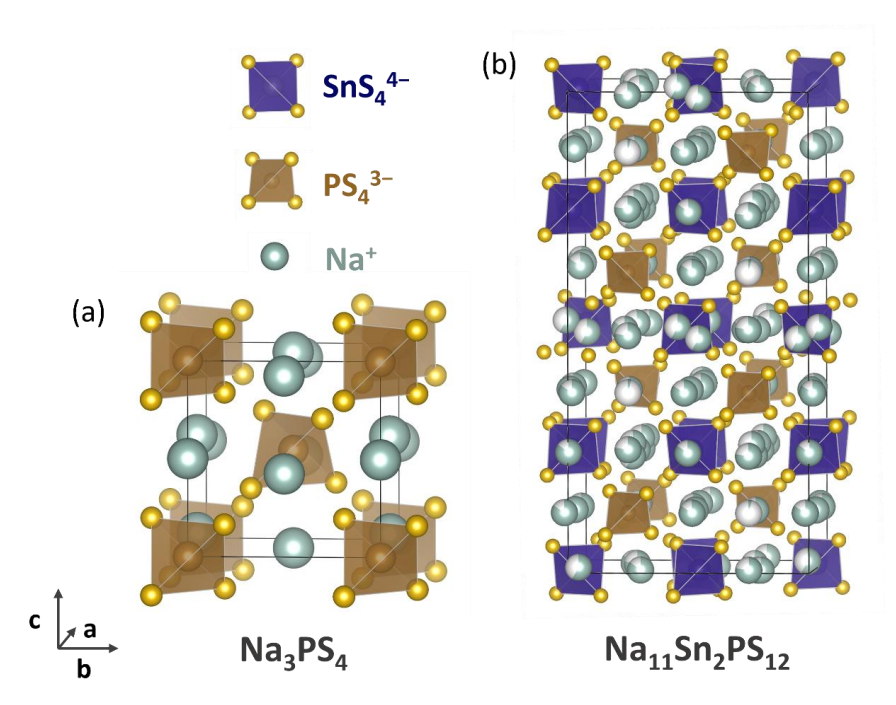


**Figure 1:** a)  $Na_3PS_4$  structure type. In the tetragonal phase the  $PS_4^{3-}$  polyanions are rotated resulting in two distinct  $Na^+$  positions. b) Crystal structure of  $Na_{11}Sn_2PS_{12}$ . Substitution of  $PS_4^{3-}$  by  $SnS_4^{4-}$  results in a  $2\times2\times4$  super cell where partially occupied sodium ion positions form a three-dimensional diffusion network.

Partial aliovalent substitution of PS<sub>4</sub><sup>3-</sup> by SnS<sub>4</sub><sup>4-</sup> polyanions leads to the structurally related compound Na<sub>11</sub>Sn<sub>2</sub>PS<sub>12</sub>.<sup>28,29</sup> Its crystal structure exhibits I4<sub>1</sub>/acd space group symmetry and resembles a 2×2×4 super cell of the Na<sub>3</sub>PS<sub>4</sub> structure (**Figure 1**). The SnS<sub>4</sub><sup>4-</sup> occupies the Wyckoff 16e positions resembling a primitive structure where the PS<sub>4</sub><sup>3-</sup> polyanions occupy every second cubic void (Wyckoff 8a). The other half of quasicubic voids (Wyckoff 8b) exhibits a very low occupancy of Na<sup>+</sup> ions (Na6 position) while five additional sodium-ion positions fill the rest of the structure.<sup>30</sup> The so build-up network of distorted NaS<sub>6</sub> octahedra is partially occupied and allows fast sodium-ion transport through the structure, 31 resulting in an ionic conductivity of around 2 mS·cm<sup>-1</sup>. To further improve the ion transport in the structure, several approaches of substitution have been carried out but have not exceed the roomtemperature conductivity of Na<sub>11</sub>Sn<sub>2</sub>PS<sub>12</sub> yet.<sup>32,33</sup> Kraft et al. performed further aliovalent substitution of PS<sub>4</sub><sup>3-</sup> by SnS<sub>4</sub><sup>4-</sup> polyanions along compounds of Na<sub>11+x</sub>Sn<sub>2+x</sub>P<sub>1-x</sub>S<sub>12</sub>. <sup>34</sup> While the substitution introduces more Na<sup>+</sup> into the structure and thereby reduces the vacancy concentration, the activation energy is reduced whereas room-temperature ionic conductivity decreases. Completely substituted  $Na_{12}Sn_3S_{12}$  (=  $Na_4SnS_4$ ) with the same crystal structure was recently obtained by dehydration where the fully occupied sodium-ion substructure results in slow ionic transport and a high activation energy.<sup>35</sup> The decrease in activation energy up to Na<sub>11.5</sub>Sn<sub>2.5</sub>P<sub>0.5</sub>S<sub>12</sub> with an increased sodium-ion concentration might indicate a concerted migration mechanism.<sup>36</sup> However, the effect of the substitution on the microscopic diffusivity is yet to be investigated. As seen in the structurally related materials, the local structure might be affected by the substitution and the diffusion mechanism remains unknown.

Inspired by the findings of different local and average structure in the related Na<sub>3</sub>PS<sub>4</sub> family, <sup>23,26</sup> we present a fundamental study on the local structure and the local transport in Na<sub>11+x</sub>Sn<sub>2+x</sub>P<sub>1-x</sub>S<sub>12</sub> to shed light into these open questions. Pair distribution function analyses show that the introduced SnS<sub>4</sub><sup>4-</sup> polyanions are locally larger than detected in the average structure which leads to strain in the crystal lattice. Nuclear magnetic resonance spectroscopy and quasi-elastic neutron scattering reveal faster local diffusivity of sodium ions with higher degree of substitution at room temperature. The induced micro strain locally increases the bottleneck size and, combined with local structural frustrations, facilitates ion transport of some of the local ionic jumps. The simultaneous reduction of the polyhedral volume of other sodium ion sites may hinder the Na<sup>+</sup> diffusion network and may contribute to a decrease in the longrange ionic conductivity together with a lower vacancy concentration. This work demonstrates that partial substitution by larger polyanions causes discrepancies in the local and average structure which can have differing effects on the local and long-range sodium-ion transport.

#### 2. Results and Discussion

Effects of substitution on the local structure. To study the effects of aliovalent substitution of  $PS_4^{3-}$  by  $SnS_4^{4-}$  on the local structure and local transport, the substitution series  $Na_{11+x}Sn_{2+x}P_{1-x}S_{12}$ , with x=0, 0.125, 0.25, 0.375 and 0.5, was synthesized via the previously reported high-temperature solid-state synthesis route.<sup>34</sup> Rietveld refinements of X-ray diffraction data confirm the successful preparation of all five compounds (Figure S1a-e). Only  $Na_{11.375}Sn_{2.375}P_{0.625}S_{12}$  contains a minor content (< 3 wt.%) of an identifiable side phase with  $Na_6Sn_2S_7$ , indicative of relative  $Na_2S$  deficiency. The refined degree of substituted  $SnS_4^{4-}$ , i.e. the Sn occupancy, are in good agreement with the nominal stoichiometry (Figure S1f) showing the successful substitution of further  $SnS_4^{4-}$  into the structure.

Nuclear magnetic resonance (NMR) spectroscopy was used to probe changes in the chemical environment of the  $SnS_4^{4-}$  and  $PS_4^{3-}$  polyanions. The <sup>119</sup>Sn magic-angle spinning (MAS) NMR spectra show one set of five overlaying <sup>119</sup>Sn signals centered around 94 ppm. A possible reason for this splitting of the signals can be found in the second coordination sphere of the 16e site

(**Figure 2**a), which allows for five possible coordinations of  $P_{4-\nu}Sn_{\nu}$  ( $\nu = 0, 1, 2, 3 \text{ and } 4$ ) of the neighbouring 8a sites in substituted  $Na_{11+x}Sn_{2+x}P_{1-x}S_{12}$ . Similar splitting due to disorder in the second coordination sphere was previously observed in related anionic frameworks. 37,38 Based on these considerations, the five <sup>119</sup>Sn signals (Figure 2b) are assigned to the different Sn(16e) -  $P_{4-\nu}Sn_{\nu}(8a)$  environments. With a higher degree of substitution, peaks corresponding to higher Sn coordination increase in intensity together with a lower chemical shift of the total <sup>119</sup>Sn signal (Figure S2). The integrated areas of the deconvoluted <sup>119</sup>Sn MAS NMR spectra follow a binomial distribution as exemplarily shown for x = 0.5 in Figure 2c. It can be concluded that the substitution is mainly statistical and the introduced SnS<sub>4</sub><sup>4-</sup> polyanions do not exhibit preferential ordering. An additional <sup>119</sup>Sn signal around 71 ppm emerges with higher degrees of substitution (Figure 2b and Figure S2) corresponding to SnS<sub>4</sub><sup>4-</sup> polyanions with the central atom located at the 8a Wyckoff position. Both, the relative intensities of the five signals making up the binomial distribution of 16e Wyckoff site as well as the ratio of relative intensities of 16e/8a Wyckoff sites, can be used to calculate the sample stoichiometry and the values are in good agreement with the degree of substitution obtained from Rietveld refinements (Figure S3). More details on the <sup>119</sup>Sn MAS NMR analysis are given in the Supplementary Information. Furthermore, <sup>31</sup>P MAS NMR spectra are recorded which show a resonance at 85 ppm for the PS<sub>4</sub><sup>3-</sup> polyanions in the pristine sample (Figure S4). With increasing substitution, additional overlapping <sup>31</sup>P signals can be observed. This broadening of the <sup>31</sup>P signal indicates an increased disorder in the Na+ substructure, however, attempted deconvolution of the signals did not yield satisfactory results.

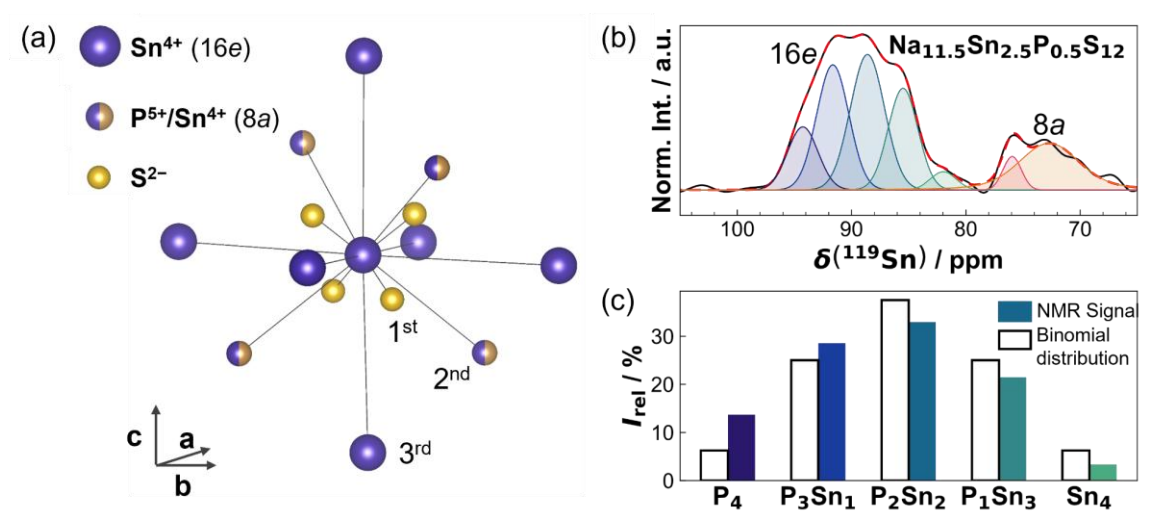


**Figure 2:** a) Schematic illustration of the three nearest coordination spheres of Sn on the Wyckoff 16e position. Substitution of  $P^{5+}$  by  $Sn^{4+}$  on the Wyckoff 8a position allows for five possible configurations for the second coordination sphere. b) <sup>119</sup>Sn MAS NMR spectra of  $Na_{11.5}Sn_{2.5}P_{0.5}S_{12}$  exhibit two broad peaks corresponding to  $Sn^{4+}$  on the Wyckoff 16e and 8a

positions. The peak for the 16e site is composed of five signals, which can be assigned to the different combination for the second coordination spheres. c) The extracted relative <sup>119</sup>Sn NMR intensities of these five different signals follow a binominal distribution showing no signs of preferential ordering of the polyanions.

To probe changes in the local structure, i.e., the short-range order, of the substituted compounds pair distribution function G(r) analyses were performed. Here, the measured X-ray total scattering data is reduced by a Fourier-transformation to obtain the G(r). It shows real-space information as a histogram of atom-atom distances which allows to investigate the local structure. The G(r) as transformed of the five compounds are compared in **Figure 3**a together with the partial contributions of the Sn-Sn, Sn-S and Sn-Na distances to the G(r) simulated from the reported structure of Na<sub>11</sub>Sn<sub>2</sub>PS<sub>12</sub>. As tin is the element with the highest electron density in the samples, these partial G(r) have the major contributions to the total pair distribution function. The first major peak corresponding to the SnS<sub>4</sub><sup>4-</sup> polyanion increases in intensity with higher substitution degree while it does not broaden significantly. For larger distances r, peaks corresponding to S-Sn and Na-S bonds broaden showing increased disorder in higher coordination spheres. Comparing the G(r) transform at different  $Q_{\text{max}}$  cut-offs confirms that these observations are not affected by transformation artefacts (Figure S5a). Using the structural model of Na<sub>11.5</sub>Sn<sub>2.5</sub>P<sub>0.5</sub>S<sub>12</sub> obtained from the Rietveld refinement of Bragg data allows to fit most signals of the G(r) reasonably well but a mismatch of the first  $SnS_4^{4-}$  peak can be observed as the Bragg model results in a broader and less intense peak (Figure S5b). This mismatch shows that the average structure obtained from X-ray diffraction cannot fully describe the local structure of  $Na_{11+x}Sn_{2+x}P_{1-x}S_{12}$ .

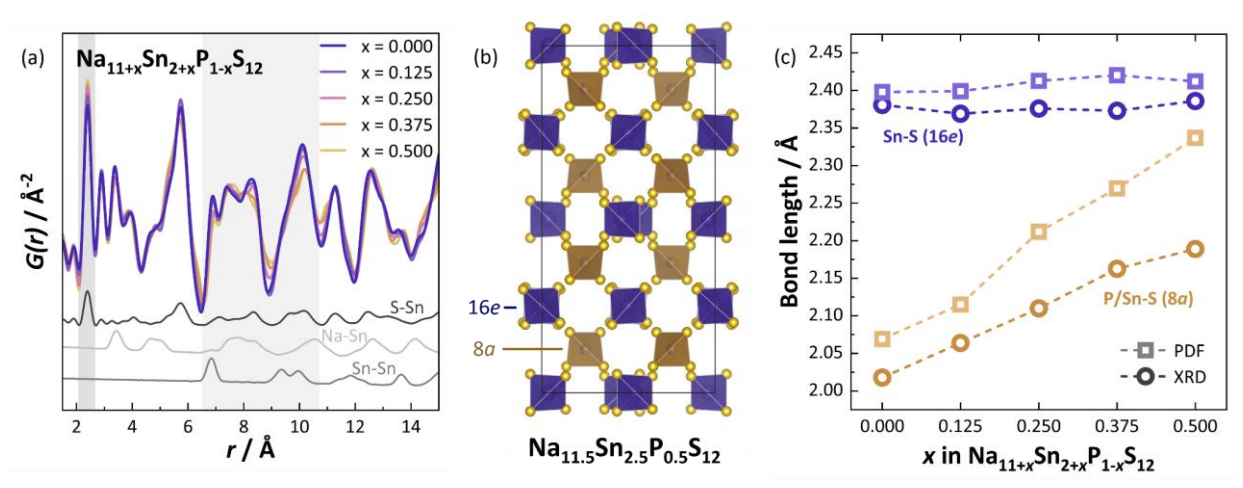


**Figure 3:** a) X-ray pair distribution functions of  $Na_{11+x}Sn_{2+x}P_{1-x}P_{1-x}Sn_{2+x}P_{1-x}P_{1-x}Sn_{2+x}P_{1-x}P_{1$ 

model of  $Na_{11.5}Sn_{2.5}P_{0.5}S_{12}$  obtained by small-box modelling of the G(r) reveals expanded polyanions on the Wyckoff 8a position. c) Comparison of the Sn/P-S bond length shows that the G(r) fit results in significantly larger polyanions on the 8a position for higher degrees of substitution than the Rietveld refinement againt Bragg data.

Utilizing the average structure to refine the G(r) by small-box modelling without restraints, results in highly distorted polyanions on the 8a position (Figure S6). In order to investigate whether the polyanions are indeed locally distorted or only differ in size compared to the average structure, small-box modelling of the G(r) was performed with restrained tetrahedral  $SnS_4^{4-}$  and  $PS_4^{3-}$  polyanions. As the stiff bonds of the polyanions exhibit much higher correlated motion than the rest of the structure the first peaks are very sharp and often not well fit by common approaches to account for correlated motion, e.g., using correlated motion factors with a dependence of 1/r or  $1/r^2$ . Several studies split the modelled r range of the G(r), however, this method does not allow to refine atomic positions for very short and longer distances simultaneously. <sup>23,40</sup> In this study, the isotropic displacement parameters are separately refined with a  $B_{\rm eq,low}$  value for the first coordination sphere and a  $B_{\rm eq,high}$  value for longer distances. Thereby, the model accounts for the strong correlated motion of the polyanions while making it still possible to refine atomic coordinates over the whole r range. Using this approach with restrained tetrahedra results in good fits of the G(r) with low residuals for all five materials (Figure S7). The anion framework of the obtained local structural model of  $Na_{11.5}Sn_{2.5}P_{0.5}S_{12}$  is shown in Figure 3b. While the SnS<sub>4</sub><sup>4-</sup>ions on the Wyckoff 16e position hardly differ from the average structure, the polyanions on the 8a position are larger in size. As Sn has a much higher atomic scattering factor, the effects of larger SnS<sub>4</sub><sup>4-</sup> ions have a more significant effect on the G(r) than the PS<sub>4</sub><sup>3-</sup> anion. Figure 3c reveals differences between the Sn-S bond distances in the average structure obtained from X-ray diffraction and the local structure from pair distribution function analysis. For the distance in the SnS<sub>4</sub><sup>4-</sup> polyanion on the 16e position there is only a slight systematic gap between the models fitted against the G(r) and Bragg data, whereas the Sn/P-S bond lengths on the 8a position diverge significantly for higher degrees of substitution. While the small-box model has its limitations and a mixed occupation of larger SnS<sub>4</sub><sup>4-</sup> and smaller PS<sub>4</sub><sup>3-</sup> polyanions on the Wyckoff 8a position is more likely than uniformly increasing polyanions, these results demonstrate that incorporated SnS<sub>4</sub><sup>4-</sup> polyanions are locally bigger than the averaged polyanion size suggested by Rietveld refinements. Clearly, by adding more  $SnS_4^{4-}$  polyanions into  $Na_{11+x}Sn_{2+x}P_{1-x}S_{12}$ , the local structure around the Wyckoff 8a position deviates more from the average structure.

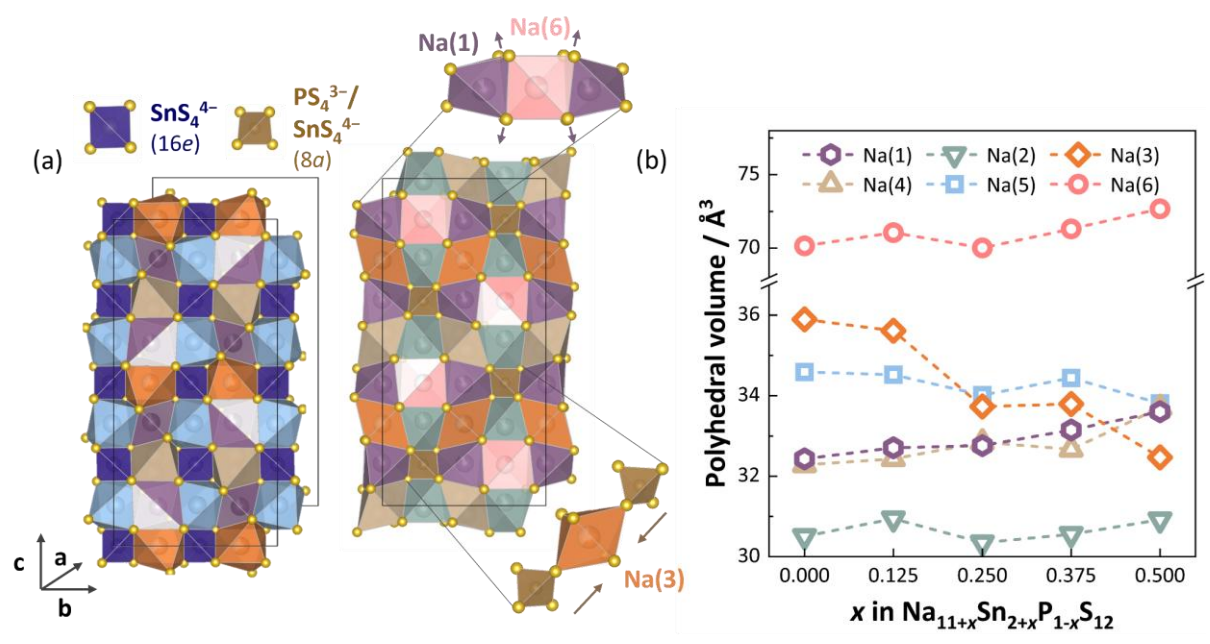


**Figure 4:** a) Sodium-ion coordination polyhedral network in  $Na_{11+x}Sn_{2+x}P_{1-x}S_{12}$  as a bilayer stack with a total of six different  $Na^+$  positions. b) Volumes of the six sodium polyhedra obtained from small-box modelling of the G(r). With higher degree of substitution the volume of Na(1) and Na(6) increase, while the volume of Na(3) significantly decreases due to larger  $SnS_4^{4-}$  polyanions on the Wyckoff 8a position.

As the G(r) show local differences in the size of the polyanions, the question arises how these affect the sodium-ion substructure and the bottlenecks of ionic transport. The Na<sub>11</sub>Sn<sub>2</sub>PS<sub>12</sub> structure-type consists of six different sodium-ion sites building a three-dimensional network for Na<sup>+</sup> diffusion (**Figure 4**a).<sup>31</sup> The substitution of PS<sub>4</sub><sup>3-</sup> by SnS<sub>4</sub><sup>4-</sup> has different effects on the volume of each sodium-ion polyhedron (see Figure 4b). The polyhedral volume of the distorted Na(1) and the low-occupied, quasicubic Na(6) polyhedron increase with higher degree of substitution. It can be explained by the expansion of the structure and lattice parameter as the similar trend is observed for the reported average structure.<sup>34</sup> As also seen in the average structure, the polyhedral volume of the Na(3) site decreases with the degree of substitution. However, in the model for the local structure the decrease is significantly more pronounced (Figure S8a). The Na(3) octahedron is linking two polyanions on the Wyckoff 8a position and shrinks as the polyanions expand and, therefore, is the most affected by the larger size of SnS<sub>4</sub><sup>4-</sup> in the local structure. As the positional coordinates of the sodium-ions are highly correlated in the G(r) modelling, no significant trends for the distortion indices of the Na<sup>+</sup> polyhedra can be observed (Figure S8b).

While the low r range of the G(r) represents the local structure, the decay of intensity towards higher distances gives information about the coherence within the material crystallites. With

increasing degree of substitution, a more pronounced decay of the G(r) can be observed. Fitting the decay with an envelope function using a spherical particle model to estimate the coherence length results in a minor decrease in coherence within the substitution series (Figure S9). This loss in coherence can also be observed in broadened reflections in the Bragg data where the broadening increases towards higher scattering vectors Q (Figure 5a). By analyzing the angle-dependence of the integral breadth of the reflections within Rietveld refinements, <sup>41</sup> the contributions of crystallite size and strain were deconvoluted. Figure 5b reveals that the crystallite size runs into the upper limit of the method and does not change whereas the  $\varepsilon_0$  value, <sup>42</sup> representing the micro strain in the material, continuously increases with higher degree of substitution. This increased strain can be related to the observed differences in the local structure and is the reason for the systematic broadening of Bragg reflections.  $\mathrm{SnS_4}^{4-}$  and  $\mathrm{PS_4}^{3-}$  polyanions on the 8a position – that are locally larger or smaller, respectively, than the average lattice site – can cause inhomogeneous strain in the structure as schematically displayed in Figure 5c.

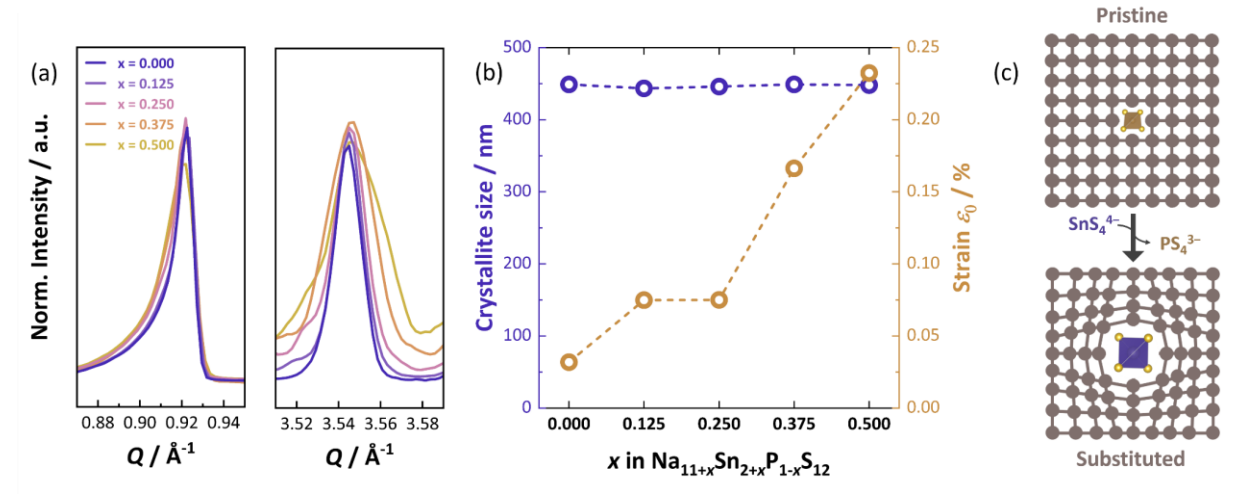


**Figure 5:** a) Bragg reflections exhibit broadening with higher degrees of substitution in  $Na_{II+x}Sn_{2+x}P_{I-x}S_{12}$  which increases as a function of Q showing changes in the microstructure. To better compare the peak shapes, reflections of substituted compounds are shifted to the respective Q value of x = 0. b) Crystallite size and strain contributions obtained from the angle-dependence of the broadening of Bragg reflections within Rietveld refinements. c) Schematic illustration how the local substitution of  $PS_4^{3-}$  by larger  $SnS_4^{4-}$  polyanions creates micro strain in the average lattice.

Effects on the local ionic transport. As the substitution by  $SnS_4^{4-}$  polyanions has different effects on each sodium-ion position, the question arises how the local transport in the  $Na_{11+x}Sn_{2+x}P_{1-x}S_{12}$  substitution series develops. <sup>23</sup>Na magic-angle spinning nuclear magnetic resonance (NMR) was carried out to probe the local chemical environment of the sodium ions.

The broad asymmetric <sup>23</sup>Na resonance signal (**Figure 6**a) for the pristine Na<sub>11</sub>Sn<sub>2</sub>PS<sub>12</sub> results from overlapping contributions from different Na<sup>+</sup>-sites with similar chemical shifts. With increasing degree of Sn-substitution, the <sup>23</sup>Na resonance signal gradually narrows - indicating an increase of the exchange rate between different Na<sup>+</sup> sites, leading to an average chemical shift with more symmetric lineshape. It can therefore be concluded that the local diffusivity at room temperature increases with the substitution of PS<sub>4</sub><sup>3-</sup> by SnS<sub>4</sub><sup>4-</sup>. To further quantify the diffusivity,  $^{23}$ Na spin-lattice ( $T_1$ ) relaxometry experiments were performed. Based on the theory of Bloembergen, Purcell and Pound (BPP), a maximum in spin-lattice relaxation rate  $(T_1^{-1})$  is observed when the jump frequency of the nuclei equals the Larmor frequency. 43 NMR spinlattice relaxometry can probe ion jumps in the MHz to GHz regime depending on the Larmor frequency  $(v_L)$  and jump frequency  $(1/\tau)$  of the mobile nucleus at the given magnetic field strength ( $v_L = 79.39$  MHz for <sup>23</sup>Na, at a magnetic field  $B_0 = 7.05$  T), i.e., the maximum of the BPP relaxation rate curve is located at  $v_L \cdot \tau \approx \frac{1}{2\pi}$ .<sup>44</sup> While a hint of the maximum seems to be observable for  $x \le 0.125$ , no resolved maximum and high-temperature flank was observed for Na<sub>11+x</sub>Sn<sub>2+x</sub>P<sub>1-x</sub>S<sub>12</sub> within the available temperature range of the NMR set-up, making it impossible to obtain reliable jump times and diffusion coefficients from the BPP model. Nevertheless, the slope of the low temperature flank of the BPP fit allows the extraction of activation energies (see Figure S10). To exclude possible effects from an asymmetric maximum lying beyond the current temperature range, the analysis is restricted to the linear part of the low temperature flank and only the six lower-temperature data points have been used with a fixed asymmetry parameter  $(\beta)$  value of 1 for the BPP fit. The so-obtained activation energies for local ionic jumps decrease with higher degree of substitution.

Quasi-elastic neutron scattering (QENS) is an additional method to quantify the microscopic diffusivity and further allows to gain information about diffusion processes and jump distances. When neutrons interact with solids they can exchange energy with lattice vibrations and diffusing ions.<sup>45</sup> While the interaction with quantized phonons results in discrete peaks of inelastic scattering, relatively small amounts of energy are transferred with diffusing ions only leading to a broadening of the elastic peak, the so-called quasi-elastic neutron scattering. The recorded QENS spectra of the five compounds (Figure S11) show an increasing quasi-elastic broadening with higher temperatures which is most pronounced for Na<sub>11</sub>Sn<sub>2</sub>PS<sub>12</sub>. For translational diffusion of ions, molecules or atoms, the half-width at half maximum  $\Gamma$  of the quasi-elastic broadening is a function of the scattering vector Q. For the self-diffusion of free moving ions  $\Gamma$  exhibits a squared dependance of Q.<sup>46</sup> In solids, ions can only jump to defined

lattice positions and the quasi-elastic broadening reaches a maximum which is described by the Chudley-Elliott model and allows the quantification of the diffusivity.<sup>47</sup> Similar to NMR spinlattice relaxometry, QENS probes local diffusion with jump frequencies in the MHz to GHz range. 48,49 The spectra were fit by the experimentally determined elastic resolution function and a Lorentzian function to account for the quasi-elastic broadening (Figure S12). The extracted values of  $\Gamma$  at 600 K as a function of Q are depicted in Figure 6b and their behavior can be described by the Chudley-Elliott model for all compounds. Due to the very low incoherent neutron scattering cross section of phosphorus, sulfur and tin, the detected quasi-elastic scattering stems almost exclusively from the scattering of diffusing sodium ions. As this model is based on uncorrelated ionic jumps between equidistant lattice sites, the QENS data does not give indications for correlated diffusion processes. Fitting the Chudley-Elliott model to the  $\Gamma$ -Q data (Figure S13) determines the mean residence time  $\tau$  (Figure S14a) and the jump distance d (Figure S14b). The obtained jump distances at 600 K increase with the substitution of PS<sub>4</sub><sup>3-</sup> by SnS<sub>4</sub><sup>4-</sup>. These values follow the trend of increased lattice parameters and are slightly higher than the average crystallographic Na<sup>+</sup>-Na<sup>+</sup> distances of 3.45 - 3.5 Å as observed in the structurally related Na<sub>2.9</sub>W<sub>0.1</sub>Sb<sub>0.9</sub>S<sub>4</sub>. For measurements at 500 K and 400 K, the obtained junp distances have relatively high uncertainties and no consistent trend with the degree of substitution is observed.

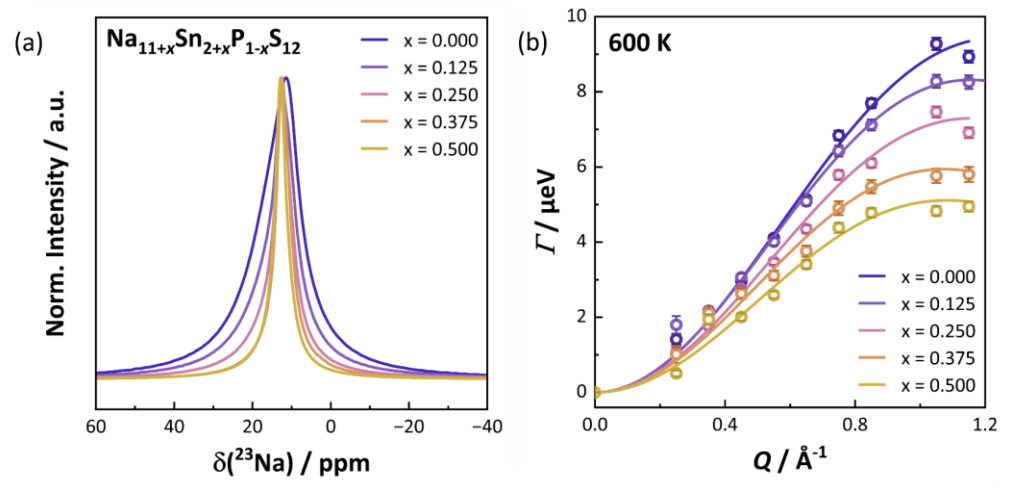


**Figure 6:** a) <sup>23</sup>Na MAS NMR spectra of  $Na_{11+x}Sn_{2+x}P_{1-x}S_{12}$  show line narrowing with higher substitution degree at room temperature. b) Quasi-elastic broadening  $\Gamma$  fitted by the Chudley-Elliott model reveal faster local diffusivity for pristine  $Na_{11}Sn_2PS_{12}$  at 600 K.

Slower ion dynamics lead to lower broadening and cause these higher uncertainties. While the maximum broadening  $\Gamma_{\text{max}}$  correlating with  $\tau$  can still be well determined, the analysis of jump distances depending on the shape of the curves is less reliable. Calculating the diffusion

coefficients D according to the random-walk theory (Equation 3) from the Chudley-Elliott model exhibit large uncertainties at lower temperature as consequence of the fluctuating jump distances (Figure S14c). For a more reliable comparison at the different temperatures, crystallographic Na<sup>+</sup> - Na<sup>+</sup> distances d (Table S7) were therefore used to calculate the microscopic diffusion coefficient. The crystallographic distances at higher temperature were extracted by using the coefficients of thermal expansion of Na<sub>11+x</sub>Sn<sub>2+x</sub>P<sub>1-x</sub>S<sub>12</sub>. To validate this approach, diffusion coefficients were also determined from linear regression of  $\Gamma$  against  $Q^2$  as the Chudley-Elliott model approaches the self-diffusion model for low Q values (Figure S15). The so obtained diffusion coefficients at 600 K are in good agreement with the respective diffusion coefficients calculated from crystallographic Na<sup>+</sup> - Na<sup>+</sup> distances. Furthermore, the values which are purely based on the Chudley-Elliott model show a similar trend corroborating the reliability of this analysis approach (Figure S15c).

Figure 7a displays the resulting diffusion coefficients of  $Na_{11+x}Sn_{2+x}P_{1-x}S_{12}$ . At 600 K the local diffusivity measured by QENS decreases with higher substitution degree. This trend seems to contrast with the observed line narrowing in the <sup>23</sup>Na NMR spectra at room temperature. However, the differences in the diffusion coefficients determined by QENS decrease at 500 K and are not observable at 400 K. Due to a too low quasi-elastic broadening, the diffusion coefficient at 300 K could not directly be determined. By extrapolating the temperature-dependent diffusion coefficients to the room-temperature values assuming Arrhenius-behavior, the diffusion coefficients at room temperature can be obtained. These diffusivities increase with the substitution by  $SnS_4^{4-}$  polyanions from  $1.6 \cdot 10^{-11}$  m<sup>2</sup>s<sup>-1</sup> to  $2.7 \cdot 10^{-11}$  m<sup>2</sup>s<sup>-1</sup> which is in line with the observed line narrowing in NMR. The trend in the local diffusivities reverses from room temperature to higher temperatures due to the different activation energies.

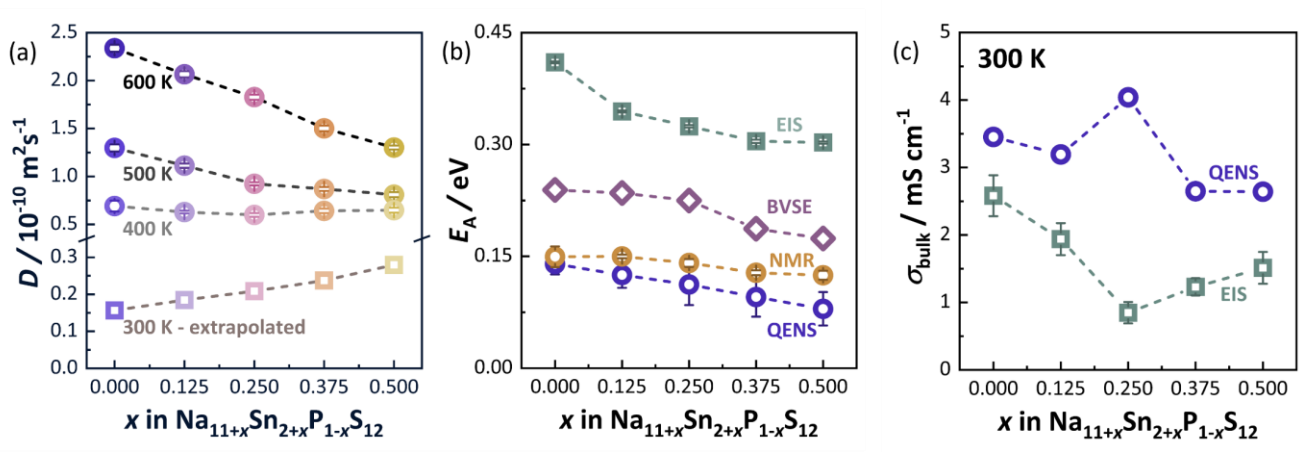


**Figure 7:** a) Diffusion coefficients calculated from the Chudley-Elliott results and the average crystallographic  $Na^+$ - $Na^+$  distance. While the diffusivity at 600 K decreases with higher

substitution degree, the trend reverses for 300 K which is extrapolated from the Arrhenius-behavior. b) Activation energies of fast localized jumps probed by QENS and NMR compared to in-grain ionic transport detected by electrochemical impedance spectroscopy (EIS). Bond valence site energies, calculated from the local structure models, show a similar trend for the the jump with the lowest activation barrier (Na(1) to Na(6) site). c) Calculated microscopic conductivities from the diffusion coefficients determined by QENS compared to the bulk ionic conductivities of  $Na_{11+x}Sn_{2+x}P_{1-x}Sn_{2}$  from impedance spectroscopy.

From the Arrhenius data of the diffusion coefficients (Figure S16), activation energies are obtained which exhibit a similar trend with those extracted from NMR relaxometry (Figure 7b). While the absolute values for the pristine sample are almost identical, the activation energies obtained by QENS have a slightly larger decrease with higher degrees of substitution. These slight deviations can be explained, considering that the small number of temperature points for the QENS measurements lead to larger uncertainties. Furthermore, the maximum of the BPP plot was not detected in the available temperature range of NMR measurements and only the low temperature flank can be used to approximate the activation energy. Nevertheless, both techniques demonstrate that the energy barrier for local jumps decreases with the aliovalent substitution. The local transport can be further compared to electrochemical impedance spectroscopy (EIS) results.<sup>34</sup> In contrast to the microscopic diffusion, macroscopic transport can be affected by the microstructure of the materials. The measured impedance spectra of  $Na_{11+x}Sn_{2+x}P_{1-x}S_{12}$  exhibit large contributions of grain boundary resistences. To obtain information about long-range transport within the grains, the samples were sintered and measured at low temperatures to allow for deconvolution of bulk and grain boundary contributions to the total resistance. Therefore, an equivalent circuit model of two series of elements consisting of a resistance in parallel with a constant phase element were employed (Figure S17a). The activation energy for the in-grain ionic transport is determined from Arrhenius-plots (Figure S17b) of the deconvoluted bulk ionic conductivities. The resulting activation energies decrease with higher degree of substitution which is in line with the results from QENS and NMR. Furthermore, the absolute values for the activation energy from impedance spectroscopy are significantly higher than those of QENS and NMR. While the latter mentioned methods detect fast local jumps without an applied field, impedance spectroscopy probes ionic transport over a longer distance with applied electric fields leading to this frequently seen difference in activation energy. 48 For the impedance spectra at room temperature, the bulk and grain boundary contributions cannot be deconvoluted (Figure S17c). Therefore, the bulk ionic conductivity at room temperature is determined by extrapolation of the Arrhenius behavior as previously done for this class of material.<sup>29,32</sup> The so-obtained ingrain ionic conductivities at room temperature decrease with higher substitution degree (Figure 7c) contrasting with the trend observed for the local diffusivities. To better compare local and long-range ionic transport, a microscopic conductivity can be calculated based on the Nernst-Einstein equation:

$$\sigma = \frac{n_{\rm c} \, q^2 D}{k \, T} \tag{1}$$

This equation relates the microscopic diffusion coefficient D with the ionic conductivity  $\sigma$  at a given temperature T using the Boltzmann constant k and the charge carrier concentration n<sub>c</sub>. <sup>48</sup> A reasonable estimate for the charge carrier concentration is the fraction of mobile Na<sup>+</sup> ions in the material (Figure S18) which can be obtained from the ratio of quasi-elastic to elastic neutron scattering intensity, weighted by the respective incoherent neutron cross sections. With increasing temperature a higher fraction of sodium ions exhibits quasi-elastic scattering. At each temperature, the amount of mobile ions decreases with the degree of substitution, showing the same trend as the vacancy concentration due to the aliovalent substitution. Using the mobile ion concentration at the lowest measured temperature (400 K) and the diffusion coefficients from QENS, the microscopic conductivity at room temperature was calculated according to Equation 1 (Figure 7c). The obtained values are slightly higher but in the same order of magnitude as the ionic conductivities determined by impedance spectroscopy, demonstrating the consistency of the transport analyses. The deviations in their absolute value may be explained by a lower charge carrier concentration at 300 K than used for the calculation and by the earlier described difference in probed local and long-range transport. Both conductivity curves, however, show a similar decrease with higher substitution degree. Only for x = 0.25 the trend deviates due to a higher fraction of mobile sodium ions. Hence, the differences in the charge carrier concentration are a major reason for the opposite trend of ionic conductivity and local diffusion coefficient at room temperature.

The question arises how the detected changes in the local structure and Na<sup>+</sup> polyhedral volume are connected to the measured local and long-range transport. The individual sodium-ion sites (Figure S19) exhibit different trends between their polyhedral volumes and the diffusion coefficient at room temperature. In particular for the Na(1) and Na(4) position, a positive correlation between local diffusivity and the larger polyhedral volume indicates an increasing bottleneck size. Bond valence site energy calculations (see Figure S19) of the local structural models show that the activation energy for the Na(1) to Na(6) jump is the lowest of all possible

jumps and exhibits a similar decrease with higher substitution compared to the activation energies detected by QENS and NMR. As the Na(6) site is energetically metastable Na(6)-Na(2) jump exhibits a higher activation barrier in these models which would indicate fast backand-forth jumps between the Na(6)-Na(1) sites. However, the Q-dependence of the Chudley-Elliott model stems from translational diffusion. While first principle calculations suggest that the Na(6) site is energetically unfavored and diffusion via a Na(1) – Na(6) – Na(1) pathway does not play a major role in Na<sub>11</sub>Sn<sub>2</sub>PS<sub>12</sub>, <sup>31,36,50</sup> the activation barrier for other jumps from the Na(1) also decrease with substitution (Figure S20) and may contribute to the decrease in the local activation energy. In contrast to the Na(1), Na(4) and Na(6) site, the polyhedral volume of other sodium ion positions decreases with higher degree of substitution due to the larger SnS<sub>4</sub><sup>4-</sup> polyanions, in particular for the Na(3) site. Here, the bond valence site energy calculations predict a higher activation energy in Na<sub>11.5</sub>Sn<sub>2.5</sub>P<sub>0.5</sub>S<sub>12</sub> for the jump between the Na(3) site and the interstitial site  $i_1$  than in the pristine material (Figure S20). The values indicate that with the locally larger  $SnS_4^{4-}$  polyanions the bottleneck size of jumps from and to the Na(3) site decreases leading to a larger activation energy. These higher local activation barriers may be detrimental for the three-dimensional diffusion network and long-range transport and may contribute to the observed lower ionic conductivities by impedance spectroscopy in addition to the lower vacancy concentration. The BVSE calculations show the reduction and increase of the activation barrier depending on the diffusion pathway. As the number of sites with increasing and decreasing polyhedral volume is similar, the averaged polyhedral volume of the local structure model exhibits no monotonous or reasonable trend with the local roomtemperature diffusivity and activation energies is observed (Figure S21).

To summarize the investigation of local structure and transport, **Figure 8**a shows the major trends that are observed with aliovalent substitution in  $Na_{11+x}Sn_{2+x}P_{1-x}S_{12}$ . The diffusion coefficient at room temperature probed by QENS increases with higher substitution degree, whereas impedance spectroscopy observes a lower long-range bulk ionic conductivity. These differences can be explained by a decrease in the concentration of mobile ions with substitution due to a reduction in the vacancy concentration  $c_v$  with substitution. Furthermore, the BVSE calculations show opposite trends in the activation barrier for different sodium ion jumps. These dissimilar diffusion pathways of (confined) local transport and long-range ion migration can further explain the contrasting trends of diffusivity and ionic conductivity which has been reported in proton conductors. X-ray diffraction and pair distribution function analysis further show that the substitution by larger  $SnS_4^{4-}$  polyanions leads to micro strain and local inhomogeneities in the structure. Figure 8b suggests that the increased strain in the material

correlates with the lower activation energy for local ionic jumps determined by QENS. Similar correlations between increased strain and improved ionic transport have been found in other ionic conductors. S2,53 In Na<sub>11+x</sub>Sn<sub>2+x</sub>P<sub>1-x</sub>S<sub>12</sub>, multiple effects of the strain on the ionic transport are possible. 1) The strain stemming from larger polyanions basically results in local expansions of the lattice, decreasing the energy of the transition state for individual jumps. 2) An additional reason may speculatively be derived from the reported concept of frustrated energy landscapes. The induced strain results in local structural frustrations where equilibrium sites of sodium ions are less stabilized and exhibit higher energetic states than in the non-strained material. As a consequence, the activation energy as the difference of the transition state and ground state decreases which is schematically depicted in Figure 8c. These local frustrations in combination with wider bottlenecks of ionic jumps should result in a flattening of the energy landscape with lower activation barriers, and the reduced local activation energies found here do show this correlation with the observed strain.

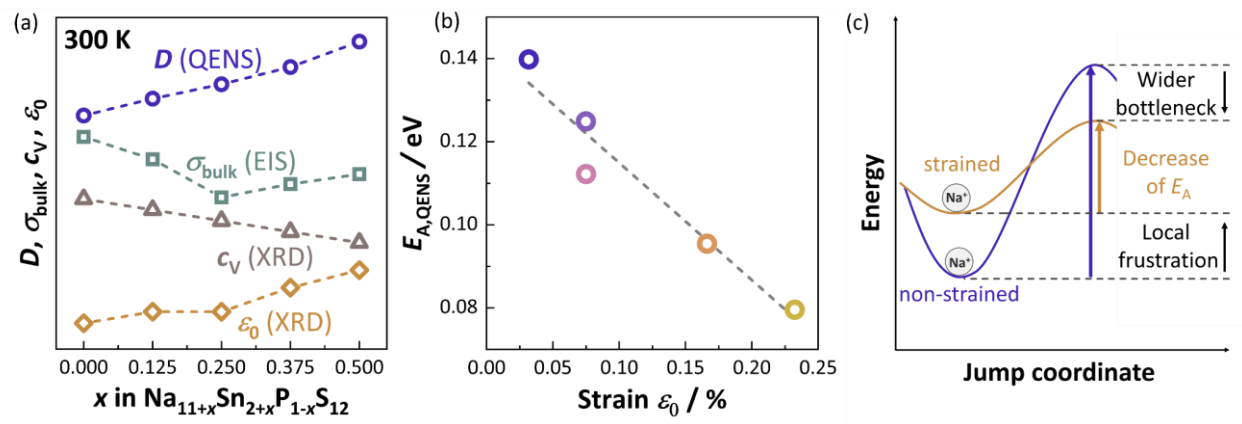


**Figure 8:** a) Summary of the observed trends for the local diffusion coefficient, bulk ionic conductivity, vacancy concentration and strain in  $Na_{11+x}Sn_{2+x}P_{1-x}S_{12}$ . b) Activation energies of local jumps determined by QENS decrease with larger micro strain caused by the substitution. c) Schematic illustration how micro strain may reduce the activation barrier for ionic jumps. Local increase of bottleneckthe local structural frustrations due to elevate the energy of equilibrium sites.

## 3. Conclusions

Investigating the  $Na_{11+x}Sn_{2+x}P_{1-x}S_{12}$  substitution series by pair distribution function analyses reveals differences in the local and average crystal structure. The substitution of  $PS_4^{3-}$  by the larger  $SnS_4^{4-}$  polyanions leads to locally inhomogeneous polyanion sizes on the Wyckoff 8a site and causes micro strain in the material. These local changes have mixed effects on the sodium ion substructure. The increase in unit cell volume results in larger Na(1) and Na(6)

polyhedra that correlate with faster local ionic transport at room temperature as NMR and QENS showed. Simultaneously, a decreasing volume of the  $Na(3)S_6$  polyhedron may hinder some pathways in the sodium ion diffusion network and reduce the long-range ionic conductivity. The induced micro strain causes local structural frustrations in the structure which can reduce the activation energies of individual jumps in combination with local expansions of the structure. While the focus for substitutions of solid electrolytes is mainly on increasing the size of bottlenecks and improving the vacancy concentration, it is often overlooked that differently sized polyanions can lead to inhomogeneities in the local structure and induce micro strain. This work demonstrates how investigating the local structure and microscopic diffusivity can help to better understand ionic conductors with complex diffusion networks. Developing strategies to engineer the microstructure of solid electrolytes will help to achieve high-performing solid-state batteries.

# 4. Experimental section

Solid-state synthesis of  $Na_{11+x}Sn_{2+x}P_{1-x}S_{12}$ . Samples with the compositions of x = 0, 0.125, 0.25, 0.375 and 0.5 were prepared according to the reported solid-state synthesis.<sup>34</sup> Stoichiometric amounts of Na<sub>2</sub>S (Merck, 99.9%), P<sub>2</sub>S<sub>5</sub> (Merck, 99%) and SnS<sub>2</sub> (Kojundo, 99.9%) were ground in a mortar for 15 min under inert conditions ( $p(O_2) < 0.1$  ppm,  $p(H_2O) < 1$  ppm) and pelletized. The pellets were sealed in evacuated quartz ampoules which were dried before under dynamic vacuum at 1073 K for two hours. The ampoules were heated up to 923 K in a horizontal tube furnace with a heating rate of 40 K per hour and were kept at the temperature for 12 hours before they were cooled down to room temperature at a cooling rate of 60 K per hour.

*X-ray total scattering.* Sample handling for every measurement was carried out under inert condition ( $p(O_2) < 0.1$  ppm,  $p(H_2O) < 1$  ppm ). X-ray total scattering data were recorded using a Stoe STADI P diffractometer (Ag K<sub> $\alpha$ 1</sub> radiation:  $\lambda = 0.55941$  Å, Ge (111) monochromator) in Debye-Scherrer geometry with four Dectris MYTHEN2 1K detectors as described by Thomae *et al.*<sup>55</sup> The samples were measured in sealed glass capillaries over a *Q*-range of 0.8-20.5 Å<sup>-1</sup> for 24 h.

Rietveld analyses. Rietveld refinements of the Bragg data were carried out using TOPAS-Academic V7.  $^{56}$   $R_{\rm wp}$  and  $R_{\rm exp}$  were used as fit indicators to assess the quality of the refinement. Due to the long measurement time and high statistics, relatively high goodness of fit (>2) ratios were obtained for all refinements. The profile of a NIST® SRM® c660 LaB<sub>6</sub> standard measurement was fitted against using a Thompson-Cox-Hastings pseudo-Voigt function to

determine the instrumental resolution function. The profile of the XRD data of each sample was refined by (1) a scale factor, (2) 10 free background coefficients of a Chebyshev polynomial function, (3) a full axial model to account for the asymmetry of the peak due to axial divergence as described by Cheary *et al.*,<sup>57</sup> (4) a zero-point offset and (5) the lattice parameters. With the determined instrumental resolution function, (6) the Gaussian and Lorentzian contributions of crystallite size and strain were extracted using the reported TOPAS macro.<sup>41,42</sup> With fixed profile parameters, the structural parameters; (7) the fractional atomic coordinates, (8) isotropic atomic displacement parameters and (9) site occupancies were subsequently allowed to vary during the refinement.

Pair distribution function analyses. For the pair distribution function analyses, the total scattering data were reduced using PDFgetX3 applying a Q-range cutoff of  $Q_{\rm max} = 16~{\rm \AA}^{-1.58}$  Small-box modelling was performed using TOPAS-Academic V7. To account for the highly correlated motion of the PS<sub>4</sub><sup>3-</sup> and SnS<sub>4</sub><sup>4-</sup> polyanions, the isotropic atomic displacement parameters of the first coordination shell ( $r < 3.07~{\rm \AA}$ ) were refined separately and a correlated motion factor delta1 was used for larger distances ( $r > 3.07~{\rm \AA}$ ). Using this approach, the model was subsequently refined by (1) the scale factor, (2) the correlated motion factor for  $r > 3.07~{\rm \AA}$ , (3) lattice parameters, (4) atomic positions, and (5) isotropic atomic displacement parameters. To restrain the tetrahedral form of the polyanions, the distance of Sn1 to S1 and Sn1 to S2 were restrained to the same bond length<sup>59</sup> with a penalty of  $10^6$  while the angle was restrained to the tetrahedral angle of  $109.47^{\circ}$  by a penalty of  $10^3$ . A spherical diameter model was applied to determine a coherence length from the decay of the G(r).

*Nuclear magnetic resonance spectroscopy.* Powder samples of all compositions were packed into cylindrical 4 mm zirconia rotors and magic-angle spinning (MAS) NMR spectra of  $^{23}$ Na ( $\nu_L = 132.36$  MHz) was recorded at a Bruker DSX 500 spectrometer equipped with a 11.74 T wide-bore magnet using a 4 mm Bruker MAS probe. The magic angle was calibrated using the spinning sidebands of  $^{23}$ Na resonance signal of solid NaNO<sub>3</sub>. For  $^{23}$ Na, radiofrequency pulse of 5.0  $\mu$ s at 120 W power was used as 90° pulse for single-pulse MAS experiments at a rotation frequency of 12.5 kHz and a recycle delay of 10 s.  $^{23}$ Na chemical shift scale was referenced against freshly prepared 1 M NaCl solution at 0 ppm.

Experiments for  $^{31}$ P ( $v_L = 202.56$  MHz) and  $^{119}$ Sn ( $v_L = 186.60$  MHz) were performed on a Bruker Avance NEO 500 spectrometer equipped with a 11.75 T wide-bore magnet using a 1.3 mm HFXY MAS probe. Powdered samples were prepared as described for  $^{23}$ Na in 1.3 mm zirconia rotors with the sample packed between MgO to ensure a fully filled rotor and centering

of the sample. Magic-angle calibration was performed as described for  $^{23}$ Na. Referencing of chemical shifts was performed via the  $^{1}$ H resonance of solid adamantane ( $\delta(^{1}\text{H}) = 1.85$  ppm) using the unified chemical shift scale. $^{61,62}$  Pulse optimization for  $^{31}$ P was performed on the sample achieving 90° pulses of 4.0  $\mu$ s at 25.0 W. For  $^{119}$ Sn pulse optimization was performed on solid SnO<sub>2</sub> achieving 90° pulses of 4.0  $\mu$ s as 30.1 W. Measurements were performed at a rotation frequency of 62.5 kHz using direct excitation. For  $^{31}$ P, 256 scans were accumulated with a recycle delay of 30 s. In case of  $^{119}$ Sn between 2048 scans and 3136 scans were accumulated with a recycle delay of 16 s. The recycle delays for both nuclei were experimentally determined for Na<sub>11.5</sub>Sn<sub>2.5</sub>P<sub>0.5</sub>S<sub>12</sub> to ensure full relaxation of the sample.

Variable temperature static saturation recovery experiments for  $^{23}$ Na ( $v_L = 79.39$  MHz) were performed on a Bruker Avance III 300 spectrometer connected to a wide-bore magnet of 7.05 T nominal magnetic field. A radio-frequency pulse length of 2.5  $\mu$ s at 120 W power was used as 90° pulse. Recovery delay lengths were varied from  $t_1 = 1.0 \,\mu$ s to  $t_{24} = 46.416 \,\mathrm{s}$  with three steps increment per decade. All the FIDs were Fourier-transformed to obtain frequency-domain signals which were integrated in TopSpin software. Corresponding signal intensity curves were fitted with monoexponential type saturation function with a stretching exponent in the OriginLab software package. Variable temperature data were recorded in the temperature range of 200-420 K with 20 K interval between successive measurements and 20 minutes of temperature stabilization period at each temperature. A combination of N<sub>2</sub> gas flow and electrical heating was used to regulate the temperature while regulation was done using temperature-dependent <sup>1</sup>H NMR signal-shifting of methanol (200-290 K) and ethylene glycol (320-420 K).

Quasi-elastic neutron scattering. QENS measurements were performed at the BASIS backscattering spectrometer at the Spallation Neutron Source of the Oak Ridge National Laboratory using Si111 analyzers with 6.4 Å wavelength and 60 Hz chopper operation mode. Samples (4-5 g) were filled into aluminum sample holders (1 mm-spaced double wall cylinder) and sealed mechanically with aluminum foil. The samples were in a closed-cycle refrigerator at 100 K, 400 K, 500 K and 600 K. An additional temperature step was measured for x = 0 at 300 K which resulted in a too low quasi-eleastic broadening and was omitted for the other samples. The Mantid software package was used for data reduction. The data was normalized against a vanadium standard and grouped in Q bins of width 0.1 Å<sup>-1</sup> over a range of 0.2 Å<sup>-1</sup> to 2.0 Å<sup>-1</sup> and energy bins of width 0.8 μeV over a range of -100 μeV to 100 μeV.

The reduced quasi-elastic structure factor data S(Q,E) were fitted against with the Dave software package according to Equation 1:<sup>65</sup>

$$S(Q, E) = \left(A\delta(E) + B \frac{\pi \Gamma(Q)}{\Gamma(Q)^2 + E^2}\right) \circ R(Q, E) + C(Q, E)$$
(2)

The model allows to deconvolute the quasi-elastic broadening as a Lorentzian function (second term) from  $A\delta(E)$  as the elastic contribution, R(Q,E) as the resolution function measured at 100 K, and the linear background function C(Q,E). From the Lorentzian function the half-width half-maximum  $\Gamma$  of the quasi-elastic broadening was extracted. These values were fitted by the Chudley-Elliott model (Equation 2) to obtain the jump distance d and mean residence time  $\tau$  at each temperature.<sup>47</sup>

$$\Gamma = \frac{\hbar}{\tau} \left( 1 - \frac{\sin(dQ)}{dQ} \right) \tag{3}$$

Diffusion coefficients D were calculated from the random-walk theory (Equation 3) with a dimensionality factor  $\gamma = 6$  to account for three dimensional diffusion.

$$D = \frac{d^2}{6\tau} \tag{4}$$

The fraction of mobile ions p was determined by the ratio of the integrated quasi-elastic scattering intensity  $I_{\text{quasi-elastic}}$  to the integrated elastic scattering intensity  $I_{\text{elastic}}$ , weighted by the incoherent neutron scattering cross sections  $\sigma_{\text{inc,Na}}$  and  $\sigma_{\text{inc,total}}$  of sodium ions and  $Na_{11+x}Sn_{2+x}P_{1-x}S_{12}$ , respectively.

$$p = \frac{\sigma_{\text{inc,total}}}{(11 + x)\sigma_{\text{inc,Na}}} \frac{I_{\text{quasi-elastic}}}{I_{\text{elastic}}}$$
 (5)

To compare the obtained fractions of mobile ions, the vacancy concentration  $c_V$  for each substitution degree x was determined via:

$$c_{\rm V} = \frac{\text{Vacancies per formula unit}}{\text{Total number of sodium ion sites}} = \frac{1 - x}{12}$$
 (6)

Electrochemical impedance spectroscopy. For impedance spectroscopy measurements, the powder samples were isostatically pressed at 325 MPa for 45 min and the obtained pellets were sintered for 10 min at 550 °C under vacuum in dried quartz ampoules. The pellets were sputter-coated with a 200 nm thick layer of gold and contacted with aluminum contacts in a pouch cell configuration. Impedance spectra were measured over a temperature range of 173 K to 298 K with a Novocontrol Alpha-A frequency analyzer applying a sinusoidal voltage curve with a 50 mV amplitude, which is needed to resolve high resistances in the frequency range from 10 MHz to 100 mHz. The obtained data were analyzed using the RelaxIS 3 software package.

*Bond valence sum calculations*. Bond valence site energies of mobile Na<sup>+</sup> ions were calculated using the softBV-GUI v1.3.1 software package.<sup>66</sup> The calculation of the energy landscape was based on the refined local structure models using the standard grid with a resolution of 0.1 Å and an average screening factor of 0.608594.

# **Supporting Information**

The Supporting Information contains results of Rietveld refinements, detailed information on NMR analyses, additional figures and crystallographic tables from small-box modelling of the G(r), QENS spectra and fits as well as the calculated bond valance site energies.

## **Data availability**

The recorded data of the presented measurements have been archived at https://doi.org/10.17879/24908359489.

## Acknowledgments

Funded by the European Union (ERC, DIONISOS, 101123802). Views and opinions expressed are however those of the author(s) only and do not necessarily reflect those of the European Union or the European Research Council Executive Agency. Neither the European Union nor the granting authority can be held responsible for them. The research is supported by the International Graduate School for Battery Chemistry, Characterization, Analysis, Recycling and Application (BACCARA), which is funded by the Ministry for Culture and Science of North Rhine Westphalia, Germany. We acknowledge funding from the Deutsche Forschungsgemeinschaft under project number 459785385. This research used resources at the Spallation Neutron Source, a DOE Office of Science User Facility operated by the Oak Ridge National Laboratory. The beam time was allocated to BASIS on proposal number IPTS-30542.

## References

- (1) Janek, J.; Zeier, W. G. A Solid Future for Battery Development. *Nature Energy* **2016**, *1* (9), 16141. https://doi.org/10.1038/nenergy.2016.141.
- (2) Janek, J.; Zeier, W. G. Challenges in Speeding up Solid-State Battery Development. *Nature Energy* **2023**, *8* (3), 230–240. https://doi.org/10.1038/s41560-023-01208-9.
- (3) Murugan, R.; Thangadurai, V.; Weppner, W. Fast Lithium Ion Conduction in Garnet-Type Li<sub>7</sub>La<sub>3</sub>Zr<sub>2</sub>O<sub>12</sub>. *Angewandte Chemie International Edition* **2007**, *46* (41), 7778.
- (4) Hong, H. Y.-P. Crystal Structure and Ionic Conductivity of Li<sub>14</sub>Zn(GeO<sub>4</sub>)<sub>4</sub> and Other New Li<sup>+</sup> Superionic Conductors. *Materials Research Bulletin* **1978**, *13* (2), 117–124. https://doi.org/10.1016/0025-5408(78)90075-2.
- (5) Li, X.; Liang, J.; Yang, X.; Adair, K. R.; Wang, C.; Zhao, F.; Sun, X. Progress and Perspectives on Halide Lithium Conductors for All-Solid-State Lithium Batteries. *Energy & Environmental Science* **2020**, *13* (5), 1429–1461.
- (6) Schlem, R.; Banik, A.; Ohno, S.; Suard, E.; Zeier, W. G. Insights into the Lithium Sub-Structure of Superionic Conductors Li<sub>3</sub>YCl<sub>6</sub> and Li<sub>3</sub>YBr<sub>6</sub>. *Chem. Mater.* **2021**, *33* (1), 327–337.
- (7) Tanaka, Y.; Ueno, K.; Mizuno, K.; Takeuchi, K.; Asano, T.; Sakai, A. New Oxyhalide Solid Electrolytes with High Lithium Ionic Conductivity> 10 mS Cm<sup>-1</sup> for All-solid-state Batteries. *Angewandte Chemie International Edition* **2023**, *62* (13), e202217581.
- (8) Zhang, S.; Zhao, F.; Chang, L.-Y.; Chuang, Y.-C.; Zhang, Z.; Zhu, Y.; Hao, X.; Fu, J.; Chen, J.; Luo, J.; Li, M.; Gao, Y.; Huang, Y.; Sham, T.-K.; Gu, M. D.; Zhang, Y.; King, G.; Sun, X. Amorphous Oxyhalide Matters for Achieving Lithium Superionic Conduction. *J. Am. Chem. Soc.* **2024**, *146* (5), 2977–2985. https://doi.org/10.1021/jacs.3c07343.
- (9) Gautam, A.; Ghidiu, M.; Suard, E.; Kraft, M. A.; Zeier, W. G. On the Lithium Distribution in Halide Superionic Argyrodites by Halide Incorporation in Li<sub>7-x</sub>PS<sub>6-x</sub>Cl<sub>x</sub>. *ACS Appl. Energy Mater.* **2021**, *4* (7), 7309–7315. https://doi.org/10.1021/acsaem.1c01417.
- (10) Bron, P.; Johansson, S.; Zick, K.; Schmedt auf der Günne, J.; Dehnen, S.; Roling, B. Li<sub>10</sub>SnP<sub>2</sub>S<sub>12</sub>: An Affordable Lithium Superionic Conductor. *J. Am. Chem. Soc.* **2013**, *135* (42), 15694–15697. https://doi.org/10.1021/ja407393y.
- (11) Kato, Y.; Saito, R.; Sakano, M.; Mitsui, A.; Hirayama, M.; Kanno, R. Synthesis, Structure and Lithium Ionic Conductivity of Solid Solutions of Li<sub>10</sub>(Ge<sub>1-x</sub>M<sub>x</sub>)P<sub>2</sub>S<sub>12</sub> (M= Si, Sn). *Journal of Power Sources* **2014**, *271*, 60–64.
- (12) Zhao, C.; Liu, L.; Qi, X.; Lu, Y.; Wu, F.; Zhao, J.; Yu, Y.; Hu, Y.-S.; Chen, L. Solid-state Sodium Batteries. *Advanced Energy Materials* **2018**, *8* (17), 1703012.
- (13) Guin, M.; Tietz, F. Survey of the Transport Properties of Sodium Superionic Conductor Materials for Use in Sodium Batteries. *Journal of power sources* **2015**, 273, 1056–1064.
- (14) Zhao, T.; Sobolev, A. N.; Schlem, R.; Helm, B.; Kraft, M. A.; Zeier, W. G. Synthesis-Controlled Cation Solubility in Solid Sodium Ion Conductors Na<sub>2+x</sub>Zr<sub>1-x</sub>In<sub>x</sub>Cl<sub>6</sub>. *ACS Applied Energy Materials* **2023**, *6* (8), 4334–4341.
- (15) Schlem, R.; Banik, A.; Eckardt, M.; Zobel, M.; Zeier, W. G. Na<sub>3-x</sub>Er<sub>1-x</sub>Zr<sub>x</sub>Cl<sub>6</sub>—A Halide-Based Fast Sodium-Ion Conductor with Vacancy-Driven Ionic Transport. *ACS Applied Energy Materials* **2020**, *3* (10), 10164–10173.

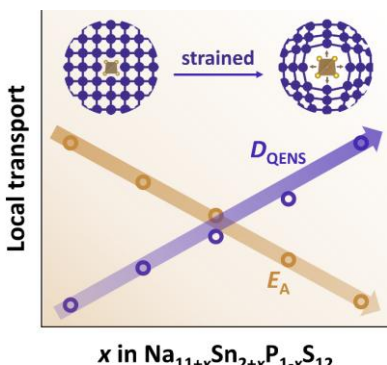
- (16) Zhou, L.; Bazak, J. D.; Li, C.; Nazar, L. F. 4 V Na Solid State Batteries Enabled by a Scalable Sodium Metal Oxyhalide Solid Electrolyte. *ACS Energy Lett.* **2024**, *9* (8), 4093–4101. https://doi.org/10.1021/acsenergylett.4c01855.
- (17) Zhao, T.; Samanta, B.; de Irujo-Labalde, X. M.; Whang, G.; Yadav, N.; Kraft, M. A.; Adelhelm, P.; Hansen, M. R.; Zeier, W. G. Sodium Metal Oxyhalides NaMOCl<sub>4</sub> (M = Nb, Ta) with High Ionic Conductivities. *ACS Materials Lett.* **2024**, *6* (8), 3683–3689. https://doi.org/10.1021/acsmaterialslett.4c01145.
- (18) Jansen, M.; Henseler, U. Synthesis, Structure Determination, and Ionic Conductivity of Sodium Tetrathiophosphate. *Journal of Solid State Chemistry* **1992**, *99* (1), 110–119. https://doi.org/10.1016/0022-4596(92)90295-7.
- (19) Jia, H.; Peng, L.; Yu, C.; Dong, L.; Cheng, S.; Xie, J. Chalcogenide-Based Inorganic Sodium Solid Electrolytes. *J. Mater. Chem. A* **2021**, *9* (9), 5134–5148. https://doi.org/10.1039/D0TA10994K.
- (20) Till, P.; Agne, M. T.; Kraft, M. A.; Courty, M.; Famprikis, T.; Ghidiu, M.; Krauskopf, T.; Masquelier, C.; Zeier, W. G. Two-Dimensional Substitution Series Na<sub>3</sub>P<sub>1-x</sub>Sb<sub>x</sub>S<sub>4-y</sub>Se<sub>y</sub>: Beyond Static Description of Structural Bottlenecks for Na<sup>+</sup> Transport. *Chem. Mater.* **2022**, *34* (5), 2410–2421. https://doi.org/10.1021/acs.chemmater.1c04445.
- (21) Famprikis, T.; Bouyanfif, H.; Canepa, P.; Zbiri, M.; Dawson, J. A.; Suard, E.; Fauth, F.; Playford, H. Y.; Dambournet, D.; Borkiewicz, O. J.; Courty, M.; Clemens, O.; Chotard, J.-N.; Islam, M. S.; Masquelier, C. Insights into the Rich Polymorphism of the Na<sup>+</sup> Ion Conductor Na<sub>3</sub>PS<sub>4</sub> from the Perspective of Variable-Temperature Diffraction and Spectroscopy. *Chem. Mater.* **2021**, *33* (14), 5652–5667. https://doi.org/10.1021/acs.chemmater.1c01113.
- (22) Hayashi, A.; Noi, K.; Sakuda, A.; Tatsumisago, M. Superionic Glass-Ceramic Electrolytes for Room-Temperature Rechargeable Sodium Batteries. *Nature communications* **2012**, *3* (1), 856.
- (23) Krauskopf, T.; Culver, S. P.; Zeier, W. G. Local Tetragonal Structure of the Cubic Superionic Conductor Na<sub>3</sub>PS<sub>4</sub>. *Inorg. Chem.* **2018**, *57* (8), 4739–4744. https://doi.org/10.1021/acs.inorgchem.8b00458.
- (24) Hayashi, A.; Masuzawa, N.; Yubuchi, S.; Tsuji, F.; Hotehama, C.; Sakuda, A.; Tatsumisago, M. A Sodium-Ion Sulfide Solid Electrolyte with Unprecedented Conductivity at Room Temperature. *Nat Commun* **2019**, *10* (1), 5266. https://doi.org/10.1038/s41467-019-13178-2.
- (25) Fuchs, T.; Culver, S. P.; Till, P.; Zeier, W. G. Defect-Mediated Conductivity Enhancements in Na <sub>3-x</sub>Pn<sub>1-x</sub>W<sub>x</sub> S<sub>4</sub> (Pn = P, Sb) Using Aliovalent Substitutions. *ACS Energy Lett.* **2020**, *5* (1), 146–151. https://doi.org/10.1021/acsenergylett.9b02537.
- (26) Maus, O.; Agne, M. T.; Fuchs, T.; Till, P. S.; Wankmiller, B.; Gerdes, J. M.; Sharma, R.; Heere, M.; Jalarvo, N.; Yaffe, O.; Hansen, M. R.; Zeier, W. G. On the Discrepancy between Local and Average Structure in the Fast Na<sup>+</sup> Ionic Conductor Na<sub>2.9</sub>Sb<sub>0.9</sub>W<sub>0.1</sub>S<sub>4</sub>. *Journal of the American Chemical Society* **2023**, *145* (13), 7147–7158. https://doi.org/10.1021/jacs.2c11803.
- (27) Brenner, T. M.; Grumet, M.; Till, P.; Asher, M.; Zeier, W. G.; Egger, D. A.; Yaffe, O. Anharmonic Lattice Dynamics in Sodium Ion Conductors. *J. Phys. Chem. Lett.* **2022**, *13* (25), 5938–5945. https://doi.org/10.1021/acs.jpclett.2c00904.

- (28) Zhang, Z.; Ramos, E.; Lalère, F.; Assoud, A.; Kaup, K.; Hartman, P.; Nazar, L. F. Na<sub>11</sub>Sn<sub>2</sub>PS<sub>12</sub>: A New Solid State Sodium Superionic Conductor. *Energy & Environmental Science* **2018**, *11* (1), 87–93.
- (29) Duchardt, M.; Ruschewitz, U.; Adams, S.; Dehnen, S.; Roling, B. Vacancy-controlled Na<sup>+</sup> Superion Conduction in Na<sub>11</sub>Sn<sub>2</sub>PS<sub>12</sub>. *Angewandte Chemie International Edition* **2018**, *57* (5), 1351–1355.
- (30) Ramos, E. P.; Zhang, Z.; Assoud, A.; Kaup, K.; Lalère, F.; Nazar, L. F. Correlating Ion Mobility and Single Crystal Structure in Sodium-Ion Chalcogenide-Based Solid State Fast Ion Conductors: Na<sub>11</sub>Sn<sub>2</sub>PS<sub>12</sub> (Pn= Sb, P). *Chemistry of Materials* **2018**, *30* (21), 7413–7417.
- (31) Sorkin, A.; Adams, S. First-Principles Study of Superionic Na<sub>9+x</sub>Sn<sub>x</sub>M<sub>3-x</sub>S<sub>12</sub> (M= P, Sb). *Materials Advances* **2020**, *1* (2), 184–196.
- (32) Duchardt, M.; Neuberger, S.; Ruschewitz, U.; Krauskopf, T.; Zeier, W. G.; Schmedt auf der Günne, J.; Adams, S.; Roling, B.; Dehnen, S. Superion Conductor Na<sub>11.1</sub>Sn<sub>2.1</sub>P<sub>0.9</sub>Se<sub>12</sub>: Lowering the Activation Barrier of Na<sup>+</sup> Conduction in Quaternary 1–4–5–6 Electrolytes. *Chemistry of Materials* **2018**, *30* (12), 4134–4139.
- (33) Kraft, M. A.; Gronych, L. M.; Famprikis, T.; Ohno, S.; Zeier, W. G. Structure and Sodium Ion Transport in Na<sub>11+x</sub>Sn<sub>2+x</sub>(Sb<sub>1-y</sub>P<sub>y</sub>)<sub>1-x</sub>S<sub>12</sub>. *Chem. Mater.* **2020**, *32* (15), 6566–6576. https://doi.org/10.1021/acs.chemmater.0c01964.
- (34) Kraft, M. A.; Gronych, L. M.; Famprikis, T.; Zeier, W. G. Influence of Reduced Na Vacancy Concentrations in the Sodium Superionic Conductors Na<sub>11+x</sub>Sn<sub>2</sub>P<sub>1-x</sub>M<sub>x</sub>S<sub>12</sub> (M = Sn, Ge). *ACS Appl. Energy Mater.* **2021**, *4* (7), 7250–7258. https://doi.org/10.1021/acsaem.1c01367.
- (35) Hartmann, F.; Benkada, A.; Indris, S.; Poschmann, M.; Lühmann, H.; Duchstein, P.; Zahn, D.; Bensch, W. Directed Dehydration as Synthetic Tool for Generation of a New Na<sub>4</sub>SnS<sub>4</sub> Polymorph: Crystal Structure, Na<sup>+</sup> Conductivity, and Influence of Sb-Substitution. *Angewandte Chemie International Edition* **2022**, *61* (36), e202202182. https://doi.org/10.1002/anie.202202182.
- (36) Zhang, Z.; Roy, P.-N.; Li, H.; Avdeev, M.; Nazar, L. F. Coupled Cation—Anion Dynamics Enhances Cation Mobility in Room-Temperature Superionic Solid-State Electrolytes. *J. Am. Chem. Soc.* **2019**, *141* (49), 19360–19372. https://doi.org/10.1021/jacs.9b09343.
- (37) Hartel, J.; Banik, A.; Gerdes, J. M.; Wankmiller, B.; Helm, B.; Li, C.; Kraft, M. A.; Hansen, M. R.; Zeier, W. G. Understanding Lithium-Ion Transport in Selenophosphate-Based Lithium Argyrodites and Their Limitations in Solid-State Batteries. *Chem. Mater.* **2023**, *35* (12), 4798–4809. https://doi.org/10.1021/acs.chemmater.3c00658.
- (38) Hogrefe, K.; Minafra, N.; Hanghofer, I.; Banik, A.; Zeier, W. G.; Wilkening, H. M. R. Opening Diffusion Pathways through Site Disorder: The Interplay of Local Structure and Ion Dynamics in the Solid Electrolyte Li<sub>6+x</sub>P<sub>1-x</sub>Ge<sub>x</sub>S<sub>5</sub>I as Probed by Neutron Diffraction and NMR. *J. Am. Chem. Soc.* **2022**, *144* (4), 1795–1812. https://doi.org/10.1021/jacs.1c11571.
- (39) Jeong, I.-K.; Heffner, R. H.; Graf, M. J.; Billinge, S. J. L. Lattice Dynamics and Correlated Atomic Motion from the Atomic Pair Distribution Function. *Physical Review B* **2003**, *67* (10), 104301.
- (40) Famprikis, T.; Kudu, Ö. U.; Dawson, J. A.; Canepa, P.; Fauth, F.; Suard, E.; Zbiri, M.; Dambournet, D.; Borkiewicz, O. J.; Bouyanfif, H.; Emge, S. P.; Cretu, S.; Chotard, J.-

- N.; Grey, C. P.; Zeier, W. G.; Islam, M. S.; Masquelier, C. Under Pressure: Mechanochemical Effects on Structure and Ion Conduction in the Sodium-Ion Solid Electrolyte Na <sub>3</sub> PS <sub>4</sub>. *J. Am. Chem. Soc.* **2020**, *142* (43), 18422–18436. https://doi.org/10.1021/jacs.0c06668.
- (41) Balzar, D.; Audebrand, N.; Daymond, M. R.; Fitch, A.; Hewat, A.; Langford, J. I.; Le Bail, A.; Louër, D.; Masson, O.; McCowan, C. N.; Popa, N. C.; Stephens, P. W.; Toby, B. H. Size–Strain Line-Broadening Analysis of the Ceria Round-Robin Sample. *Journal of Applied Crystallography* **2004**, *37* (6), 911–924.
- (42) Balzar, D. Voigt-Function Model in Diffraction Line-Broadening Analysis. *Defect and microstructure analysis by diffraction* **1999**, 94–126.
- (43) Bloembergen, N.; Purcell, E. M.; Pound, R. V. Relaxation Effects in Nuclear Magnetic Resonance Absorbtion. *Phys Rev* **1948**, *731679*.
- (44) Wankmiller, B.; Hansen, M. R. Observation of Li<sup>+</sup> Jumps in Solid Inorganic Electrolytes over a Broad Dynamical Range: A Case Study of the Lithium Phosphidosilicates Li<sub>8</sub>SiP<sub>4</sub> and Li<sub>14</sub>SiP<sub>6</sub>. *Journal of Magnetic Resonance Open* **2023**, *14–15*, 100098. https://doi.org/10.1016/j.jmro.2023.100098.
- (45) Embs, J. P.; Juranyi, F.; Hempelmann, R. Introduction to Quasielastic Neutron Scattering. *Zeitschrift für Physikalische Chemie* **2010**, 224 (1–2), 5–32.
- (46) Kruteva, M. Dynamics Studied by Quasielastic Neutron Scattering (QENS). *Adsorption* **2021**, *27*, 875–889.
- (47) Chudley, C. T.; Elliott, R. J. Neutron Scattering from a Liquid on a Jump Diffusion Model. *Proc. Phys. Soc.* **1961**, 77 (2), 353–361. https://doi.org/10.1088/0370-1328/77/2/319.
- (48) Mehrer, Helmut. Diffusion in Solids. Springer 2007.
- (49) Hogrefe, K.; Stainer, F.; Minafra, N.; Zeier, W. G.; Wilkening, H. M. R. NMR Down to Cryogenic Temperatures: Accessing the Rate-Limiting Step of Li Transport in Argyrodite Electrolytes. *Chem. Mater.* **2024**, *36* (13), 6527–6534. https://doi.org/10.1021/acs.chemmater.4c00746.
- (50) Oh, K.; Chang, D.; Park, I.; Yoon, K.; Kang, K. First-Principles Investigations on Sodium Superionic Conductor Na<sub>11</sub>Sn<sub>2</sub>PS<sub>12</sub>. *Chem. Mater.* **2019**, *31* (16), 6066–6075. https://doi.org/10.1021/acs.chemmater.8b04965.
- (51) al-Wahish, A.; Jalarvo, N.; Bi, Z.; Herwig, K. W.; Bridges, C.; Paranthaman, M. P.; Mandrus, D. Quasi-Elastic Neutron Scattering Reveals Fast Proton Diffusion in Ca-Doped LaPO<sub>4</sub>. *J. Phys. Chem. C* 2014, *118* (35), 20112–20121. https://doi.org/10.1021/jp5048425.
- (52) Burbano, M.; Marrocchelli, D.; Watson, G. W. Strain Effects on the Ionic Conductivity of Y-Doped Ceria: A Simulation Study. *Journal of Electroceramics* **2014**, *32*, 28–36.
- (53) Faka, V.; Agne, M. T.; Lange, M. A.; Daisenberger, D.; Wankmiller, B.; Schwarzmüller, S.; Huppertz, H.; Maus, O.; Helm, B.; Böger, T.; Hartel, J.; Gerdes, J. M.; Molaison, J. J.; Kieslich, G.; Hansen, M. R.; Zeier, W. G. Pressure-Induced Dislocations and Their Influence on Ionic Transport in Li<sup>+</sup>-Conducting Argyrodites. *J. Am. Chem. Soc.* **2024**, *146* (2), 1710–1721. https://doi.org/10.1021/jacs.3c12323.
- (54) Wood, B. C.; Varley, J. B.; Kweon, K. E.; Shea, P.; Hall, A. T.; Grieder, A.; Ward, M.; Aguirre, V. P.; Rigling, D.; Lopez Ventura, E.; Stancill, C.; Adelstein, N. Paradigms of

- Frustration in Superionic Solid Electrolytes. *Philosophical Transactions of the Royal Society A* **2021**, *379* (2211), 20190467.
- (55) Thomae, S. L. J.; Prinz, N.; Hartmann, T.; Teck, M.; Correll, S.; Zobel, M. Pushing Data Quality for Laboratory Pair Distribution Function Experiments. *Review of Scientific Instruments* **2019**, *90* (4), 043905. https://doi.org/10.1063/1.5093714.
- (56) Coelho, A. A. TOPAS and TOPAS-Academic: An Optimization Program Integrating Computer Algebra and Crystallographic Objects Written in C++. *Journal of Applied Crystallography* **2018**, *51* (1), 210–218.
- (57) Cheary, R. W.; Coelho, A. A. An Experimental Investigation of the Effects of Axial Divergence on Diffraction Line Profiles. *Powder Diffraction* **1998**, *13* (2), 100–106.
- (58) Juhás, P.; Davis, T.; Farrow, C. L.; Billinge, S. J. L. PDFgetX3: A Rapid and Highly Automatable Program for Processing Powder Diffraction Data into Total Scattering Pair Distribution Functions. *J. Appl. Crystallogr.* **2013**, *46*, 560–566.
- (59) Dinnebier, R. E.; Leineweber, A.; Evans, J. S. Rietveld Refinement: Practical Powder Diffraction Pattern Analysis Using TOPAS; de Gruyter, 2018.
- (60) Howell, R. C.; Proffen, T.; Conradson, S. D. Pair Distribution Function and Structure Factor of Spherical Particles. *Physical Review B* **2006**, *73* (9), 094107.
- (61) Harris, R. K.; Becker, E. D.; Cabral de Menezes, S. M.; Goodfellow, R.; Granger, P. NMR Nomenclature. Nuclear Spin Properties and Conventions for Chemical Shifts(IUPAC Recommendations 2001). *Pure Appl. Chem.* **2001**, *73* (11), 1795–1818. https://doi.org/10.1351/pac200173111795.
- (62) Hayashi, S.; Hayamizu, K. Chemical Shift Standards in High-Resolution Solid-State NMR (1) 13C, 29Si, and 1H Nuclei. *Bulletin of the Chemical Society of Japan* **1991**, 64 (2), 685–687. https://doi.org/10.1246/bcsj.64.685.
- (63) Mamontov, E.; Herwig, K. W. A Time-of-Flight Backscattering Spectrometer at the Spallation Neutron Source, BASIS. *Review of Scientific Instruments* **2011**, 82 (8), 085109.
- (64) Osti, N. C.; Jalarvo, N.; Mamontov, E. Backscattering Silicon Spectrometer (BASIS): Sixteen Years in Advanced Materials Characterization. *Materials Horizons* **2024**, *11* (19), 4535–4572.
- (65) Gupta, M. K.; Ding, J.; Osti, N. C.; Abernathy, D. L.; Arnold, W.; Wang, H.; Hood, Z.; Delaire, O. Fast Na Diffusion and Anharmonic Phonon Dynamics in Superionic Na<sub>3</sub>PS<sub>4</sub>. *Energy Environ. Sci.* **2021**, *14* (12), 6554–6563. https://doi.org/10.1039/D1EE01509E.
- (66) Chen, H.; Wong, L. L.; Adams, S. SoftBV–a Software Tool for Screening the Materials Genome of Inorganic Fast Ion Conductors. *Acta Crystallographica Section B: Structural Science, Crystal Engineering and Materials* **2019**, *75* (1), 18–33.

For table of contents only.



x in Na<sub>11+x</sub>Sn<sub>2+x</sub>P<sub>1-x</sub>S<sub>12</sub>

Substitution by larger polyanions in the fast sodium ion conductor  $Na_{11+x}Sn_{2+x}P_{1-x}S_{12}$  leads to inhomogeneities in the local structure which induces micro strain. The observed strain correlates with higher local diffusivities at room temperature and a lowering of the activation barriers for local ionic jumps which is explained by a widening of structural bottlenecks and local structural frustrations.